

GMSRF-Net: An improved generalizability with global multi-scale residual fusion network for polyp segmentation

Abhishek Srivastava*, Sukalpa Chanda[†], Debesh Jha^{‡§}, Umapada Pal*, Sharib Ali[¶]
^{*}Indian Statistical Institute, India [†]Østfold University College, Norway [‡]SimulaMet, Norway
[§]UiT The Arctic University of Norway, Norway [¶]University of Oxford, UK
 Email: abhisheksrivastava2397@gmail.com

Abstract—Colonoscopy is a gold standard procedure but is highly operator-dependent. Efforts have been made to automate the detection and segmentation of polyps, a precancerous precursor, to effectively minimize missed rate. Widely used computer-aided polyp segmentation systems actuated by encoder-decoder have achieved high performance in terms of accuracy. However, polyp segmentation datasets collected from varied centers can follow different imaging protocols leading to difference in data distribution. As a result, most methods suffer from performance drop and require re-training for each specific dataset. We address this generalizability issue by proposing a global multi-scale residual fusion network (GMSRF-Net). Our proposed network maintains high-resolution representations while performing multi-scale fusion operations for all resolution scales. To further leverage scale information, we design cross multi-scale attention (CMSA) and multi-scale feature selection (MSFS) modules within the GMSRF-Net. The repeated fusion operations gated by CMSA and MSFS demonstrate improved generalizability of the network. Experiments conducted on two different polyp segmentation datasets show that our proposed GMSRF-Net outperforms the previous top-performing state-of-the-art method by 8.34% and 10.31% on unseen CVC-ClinicDB and unseen Kvasir-SEG, in terms of dice coefficient.

Index Terms—Deep learning, polyp segmentation, generalization, multi-scale feature fusion, colonoscopy

I. INTRODUCTION

Colorectal cancer (CRC) has been consistently ranked third in terms of prevalence [1]. The leading cause of CRC is colorectal adenomatous polyps, and thus identification and resection of polyps can reduce the occurrence of CRC. Colonoscopy serves as a gold standard technique for surveillance and treatment. Studies have shown that timely colonoscopy can reduce the chances of CRC by 30% [2]. However, the success of careful identification of malicious polyps and their subsequent resection depends on the ability and experience of clinicians which makes it prone to human error. Such factors eventually lead to a high polyp missed rate [3]. Artificial intelligence (AI) driven methods can be effective and provide precise detection and segmentation of polyps.

With the advent of convolution neural networks (CNNs) research for the polyp segmentation task has been widely conducted to reduce operator-dependent problems in colonoscopy. However, the variations in structures and size of polyps and fluctuation of contrast between polyps and their immediate surrounding make it a challenging task. Whilst methods such

as U-Net [4], U-Net++ [5], PraNet [6], UACA-Net [7], MSRF-Net [8] have demonstrated higher metric performances, when the intervention of imaging protocols varies, performance of these methods fall considerably. The imaging protocols used to acquire colonoscopy images at most times vary over different medical institutions, the performance drop in these methods when tested on unseen data need to be minimized.

We can observe various reincarnations of the U-Net developed for polyp segmentation task in [5], [9], [10]. Similarly, PraNet [6] aggregated deep features in their parallel partial decoder to form initial guidance area maps. ColonSegNet [11] used only two encoder and two decoder layers that made their network parameters relatively smaller enabling a faster inference time. UACA-Net [7] used a saliency map for each level in the decoder to calculate foreground, background, and uncertain area maps. However, a major drawback with encoder-decoder architectures like U-Net is that shallow features from the encoder and deep features from the decoder suffer from semantic gap [12]. Deeplabv3+ [13] introduced atrous spatial pyramid pooling with skip connections to aggregate global multi-scale context. Wang et al. [14] designed a network where spatial precision is not compromised by maintaining high-resolution representations throughout the process. Here, multi-scale fusion is performed by repeated cross-scale fusion of features for all resolution scales. Inspired by deep fusion [15], [16], MSRF-Net [8] increased the number of fusion operations by introducing dual-scale dense fusion blocks, which allowed the preservation of both high- and low-level features for all resolution scales. The authors [8] demonstrated the superior generalizability of MSRF-Net and HRNet on polyp segmentation tasks. Building upon these concepts we aim to increase generalizability of polyp segmentation task under different clinical settings by introducing a global multi-scale residual fusion network “GMSRF-Net”.

Our GMSRF-Net uses a densely connected multi-scale fusion mechanism that fuses features from all resolution scales at once. The fusion of multi-scale features occurs at each convolutional layer of the densely connected structure which further increases the frequency of fusion operation while maintaining global multi-scale context throughout the process. Additionally, we design a novel cross multi-scale attention (CMSA) mechanism. These attention maps formed

by the aggregation of multi-scale context boost the feature map representations in all resolution scales. Our multi-scale feature selection (MSFS) module, applies channel-wise attention on the features fused from all scales to further amplify the relevant features. Experiments demonstrate the improved generalizability of the proposed approach compared to former state-of-the-art (SOTA) methods. Thus, our GMSRF-Net opens new avenues to enhance the generalization capacity of CNN-based supervised learning approaches.

II. MATERIALS AND METHOD

A. Materials

We have chosen two standard publicly available polyp segmentation datasets: Kvasir-SEG [17] and CVC-ClinicDB [18]. Kvasir-SEG was acquired in Vestre Viken Health Trust in Norway while CVC-ClinicDB was obtained in Hospital Clinic in Barcelona, Spain. To demonstrate the effectiveness of our technique we perform four experiments with different setups. Two experiments were carried out when the training and testing datasets are the same. Additionally, to establish the generalization capacity of our network, we trained and tested our model on different datasets, i.e., trained on Kvasir-SEG and tested on CVC-ClinicDB and vice versa.

B. Method

In this section, we present the architecture of our GMSRF-Net (see Fig. 1). GMSRF-Net uses global multi-scale feature fusion mechanism which incorporates cross multi-scale attention and subsequent multi-scale feature selection module for accurate and generalizable segmentation of polyps. The encoder, two GMSRF modules, and decoder are detailed in the following subsections.

1) *Encoder block*: The colonoscopy images are first processed by ResNet50 [19] backbone pre-trained on ImageNet. The number of feature maps for all scales is reduced by Receptive Field Blocks (RFBs) [20] to reduce the computational cost incurred by the following global multi-scale residual fusion (GMSRF) and the decoder network (see Fig. 1(a)). Here, the features generated by the RFB module be denoted as X_i where $i \in \{1, 2, 3, 4\}$ denote scales.

2) *Global Multi-Scale Residual Fusion block*: Let $[X_1, X_2, X_3, X_4]$ denote features of distinct spatial resolutions (see Fig. 1(b)). In the initial layer $l = 1$, where l represents the layer number in GMSRF module, each set of feature maps undergoes a convolution operation with output number of feature maps set as k , k being the growth factor [21].

Cross multi-scale attention maps (CMSA) are calculated for each scale concurrently. Eq. 1 represents how the l' th CMSA is calculated for the i' th scale. $\{X_w, X_y, X_z\} \neq X_i$ are first transformed to the spatial resolution size of the i' th scale by suitable convolution or transposed convolution operations (see Fig. 2). They are concatenated and then processed by a 3×3 convolution operation, to effectively fuse the features of selected scales.

$$X_{att,i,l} = Conv_{1 \times 1}(Conv_{3 \times 3}(X_{w,l-1} \oplus X_{y,l-1} \oplus X_{z,l-1}), \{w, y, z\} \neq i) \quad (1)$$

Here, \oplus represents concatenation operation. Attention maps are then generated to identify spatial locations based on the fused multi-scale features of parallel resolution streams. The information conveyed from low-resolution streams helps to boost the feature maps in the high-resolution stream and vice versa. The subsequent combination with the CMSA module allows the selection of features that are relevant towards identifying the region-of-interest.

Global multi-scale residual fusion (GMSRF) is performed as described in Eq. (2). The l' th convolutional layer in the i' th resolution stream receives concatenated feature maps from $l - 1'$ th convolutional layer from all resolution scales and previous convolutional layers for the same resolution stream (see Fig. 1(b)). This global multi-scale fusion with densely connected blocks increases the number of paths through which feature maps can propagate and undergoes varying operations before contributing to the final segmentation map prediction.

$$X_{i,l} = Conv_{3 \times 3}(X_{i,0} \cdots X_{i,l-1} \oplus X_{w,l-1} \oplus X_{y,l-1} \oplus X_{z,l-1}), \{w, y, z\} \neq i \quad (2)$$

The feature maps can capture the global multi-scale context at each layer of the densely connected mechanism. Eq. (3) describes how CMSA maps are used to identify and propagate relevant features of the i' th scale stream forward.

$$X_{i,l} = X_{i,l} \otimes X_{att,i,l} \quad (3)$$

Multi-scale feature selection (MSFS) module, is the next step where channel-wise attention is applied on the fused features using squeeze and excitation (S&E) block [22] (refer to Fig. 2). This enables the amplification of salient channels transmitted by various scale streams. The suppression of irrelevant channels by this module is also conducive to a higher level of accuracy. Residual connection from the input of the GMSRF module is added to improve gradient flow. For simplification purposes, we use the i' th scale while describing this mechanism.

3) *Decoder*: To fully establish the contribution of our GMSRF-Net, we choose to use a vanilla decoder (see Fig. 1(a)). X_i is the output of the GMSRF module for the i' th scale. Each decoder block upscales the output from the previous decoder block and concatenates the resultant feature maps from the same scale output of the GMSRF module (see Equation 4).

$$D_i = Conv_{3 \times 3}(TransConv(D_{i-1}) \oplus X_i) \quad (4)$$

Here, TransConv is strided transposed convolutional layer and initially $D_4 = X_4$. The output of all decoder blocks, i.e D_4, D_3, D_2 , are upscaled to the size of ground truth maps for improved gradient flow and regularization.

4) *Loss Function*: We use a dual loss function $\mathcal{L}_{DUAL} = \mathcal{L}_{BCE} + \mathcal{L}_{IoU}$, where \mathcal{L}_{DUAL} is a combination of weighted intersection over union loss (\mathcal{L}_{IoU}) and binary cross entropy (\mathcal{L}_{BCE}). For all supervise segmentation maps generated by all decoder levels, the total loss function is given by: $\mathcal{L}_{GMSRF} = \sum_{i=1}^{i=4} \mathcal{L}_{DUAL}(D_i)$, where i is the number of decoder layers.

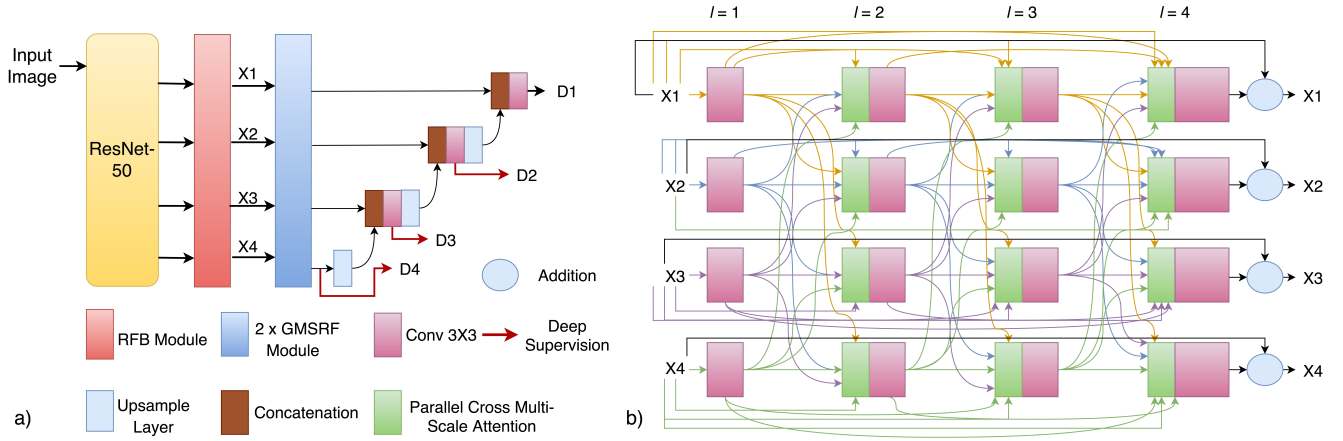


Table I: Result comparison when source dataset is Kvasir-SEG

| Method | Source data | | | | Unseen dataset "CVC-ClinicDB" | | | |
|-----------------------------|---------------|---------------|---------------|---------------|-------------------------------|---------------|---------------|---------------|
| | DSC | mIoU | Recall | Precision | DSC | mIoU | Recall | Precision |
| U-Net [4] | 0.8629 | 0.8176 | 0.9094 | 0.8901 | 0.7172 | 0.6133 | 0.7255 | 0.7986 |
| U-Net++ [5] | 0.7475 | 0.6313 | 0.6865 | 0.8871 | 0.4265 | 0.3345 | 0.3939 | 0.6894 |
| Deeplabv3+ (Xception) [13] | 0.8965 | 0.8575 | 0.8984 | 0.9496 | 0.6509 | 0.5385 | 0.6251 | 0.7947 |
| Deeplabv3+ (Mobilenet) [13] | 0.8656 | 0.8186 | 0.8808 | 0.9205 | 0.6303 | 0.4825 | 0.5957 | 0.7173 |
| HRNetV2-W18-Smallv2 [23] | 0.8179 | 0.7470 | 0.8016 | 0.8696 | 0.6428 | 0.5513 | 0.6811 | 0.7253 |
| HRNetV2-W48 [23] | 0.8896 | 0.8262 | 0.8973 | 0.9056 | 0.7901 | 0.6953 | 0.8796 | 0.7694 |
| ColonSegNet [11] | 0.8203 | 0.7435 | 0.8124 | 0.8832 | 0.6895 | 0.5813 | 0.7862 | 0.7177 |
| PraNet [6] | 0.9078 | 0.8561 | 0.9034 | 0.9352 | 0.7225 | 0.6328 | 0.7531 | 0.7888 |
| UACANet-S [7] | 0.8800 | 0.8250 | 0.8701 | 0.9229 | 0.5683 | 0.4907 | 0.5792 | 0.7095 |
| UACANet-L [7] | 0.9014 | 0.8555 | 0.8897 | 0.9381 | 0.5589 | 0.4849 | 0.5800 | 0.6775 |
| MSRF-Net [8] | 0.9217 | 0.8914 | 0.9198 | 0.9666 | 0.7921 | 0.6498 | 0.9001 | 0.7000 |
| GMSRF-Net | 0.9263 | 0.8843 | 0.9402 | 0.9310 | 0.8755 | 0.8091 | 0.9106 | 0.8588 |

Table II: Result comparison when source dataset is CVC-ClinicDB

| Method | Source data | | | | Unseen dataset "Kvasir-SEG" | | | |
|-----------------------------|---------------|---------------|---------------|---------------|-----------------------------|---------------|---------------|---------------|
| | DSC | mIoU | Recall | Precision | DSC | mIoU | Recall | Precision |
| U-Net [4] | 0.9145 | 0.8654 | 0.9178 | 0.9381 | 0.6222 | 0.4588 | 0.5129 | 0.8133 |
| U-Net++ [5] | 0.8453 | 0.7559 | 0.8917 | 0.8323 | 0.5926 | 0.4564 | 0.7352 | 0.5462 |
| Deeplabv3+ (Xception) [13] | 0.8897 | 0.8706 | 0.9251 | 0.9366 | 0.6746 | 0.5327 | 0.7757 | 0.6296 |
| Deeplabv3+ (Mobilenet) [13] | 0.8985 | 0.8588 | 0.9160 | 0.9287 | 0.6474 | 0.5098 | 0.6632 | 0.6878 |
| HRNetV2-W18-Smallv2 [23] | 0.9073 | 0.8457 | 0.9137 | 0.9191 | 0.7012 | 0.6009 | 0.7184 | 0.7666 |
| HRNetV2-W48 [23] | 0.9244 | 0.8747 | 0.9234 | 0.9296 | 0.7404 | 0.6233 | 0.7293 | 0.8511 |
| ColonSegNet [11] | 0.9132 | 0.8600 | 0.9072 | 0.9292 | 0.6324 | 0.5183 | 0.6112 | 0.7897 |
| PraNet [6] | 0.9072 | 0.8575 | 0.9227 | 0.9134 | 0.7293 | 0.6262 | 0.8007 | 0.7623 |
| UACANet-S [7] | 0.9190 | 0.8700 | 0.9285 | 0.9201 | 0.6945 | 0.5894 | 0.7692 | 0.7377 |
| UACANet-L [7] | 0.9098 | 0.8649 | 0.9174 | 0.9114 | 0.7312 | 0.6383 | 0.7417 | 0.8314 |
| MSRF-Net [8] | 0.9420 | 0.9043 | 0.9567 | 0.9427 | 0.7575 | 0.6337 | 0.7197 | 0.8414 |
| GMSRF-Net | 0.9326 | 0.8882 | 0.9376 | 0.9307 | 0.8606 | 0.7877 | 0.8641 | 0.9056 |

III. EXPERIMENTS

A. Experimental setup

We evaluate our proposed GMSRF-Net on Kvasir-SEG and CVC-ClinicDB. All images are resized to 256×256 as a pre-processing step. We reserve 80% data for training, 10% for validation, and 10% for testing. The training set is augmented using techniques like random flipping, cropping, color jittering etc. All experiments are conducted using the same train-val-test configuration. We train the network for 50 epochs using Adam optimizer with initial learning rate of $1e-4$ and batch

size of 8. All experiments were performed on an NVIDIA DGX-2 machine using NVIDIA V100.

B. Results and discussion

From Table I, it can be observed that our GMSRF-Net is competitive to MSRF-Net on the same source data (Kvasir-SEG), while outperforming on unseen data (CVC-ClinicDB). An increase of 8.34%, 15.93%, 1.05%, 15.88% in dice coefficient (DSC), mean intersection over union (mIoU), recall and precision, respectively, can be seen when compared with the best performing SOTA method (MSRF-Net). A similar

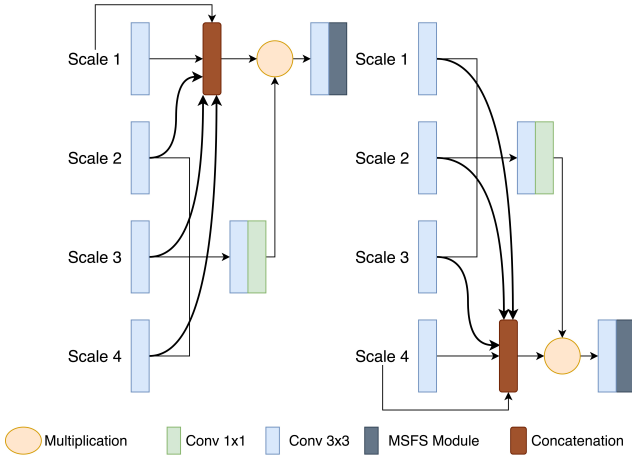


Figure 2: Computation of CMSA and MSFS for scale 1 and scale 4 (computed for scale 2 and scale 3 as well)

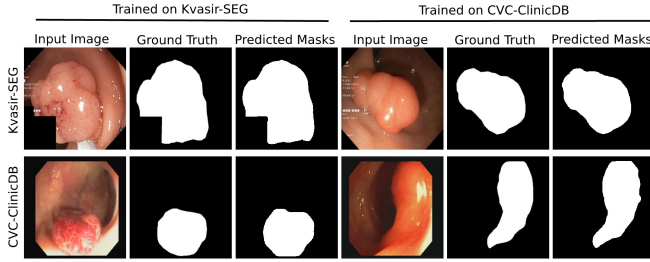


Figure 3: Qualitative results for GMSRF-Net

trend can be noted in Table II where our proposed method outperformed SOTA method on unseen Kvasir-SEG by large margins on all metrics: improvement of 10.31%, 15.40%, 14.44% and 6.42% on DSC, mIoU, recall and precision, respectively. Moreover, we can see that GMSRF-Net achieves a DSC of 0.8606 when trained on CVC-ClinicDB and tested on Kvasir-SEG (see Table II). However, some networks such as U-Net++, ColonSegNet, and HRNetV2-W18-Smallv2 reports relatively lower performance even when they are trained and tested on Kvasir-SEG (see Table II). Fig. 3 exhibits that our GMSRF-Net produces optimal segmentation mask predictions in both scenarios when training and test sources are either the same or different.

Our experiments demonstrate that the multi-scale fusion technique that combines features from all resolution scales such as HR-Net and MSRF-Net yields better generalization performances (see Table I-II). Our GMSRF-Net using global multi-scale residual fusion increases the number of fusion operations together with attention modules (CMSA and MSFS) achieving an improved generalization ability.

IV. CONCLUSION

In this paper, we propose a global multi-scale feature fusion technique that incorporates CMSA and MSFS mechanisms for aggregating reliable and robust global features at each stage. Our proposed network maintains high resolution representa-

tions and enriches high-resolution features by fusion with low-resolution feature streams and vice versa. The proposed technique achieves significant performance gain on segmentation tasks where the training and testing datasets are from different distributions. The generalization performance of our GMSRF-Net is an important step towards improving the generalizability of supervised learning methods. In future, we will extend our work towards quantifying the generalizability of the proposed model on other biomedical imaging datasets.

This research study was conducted retrospectively using human subject data made available in open access by Kvasir-SEG and CVC-ClinicDB. Ethical approval was not required.

REFERENCES

- [1] N. Howlader, A. Noone, M. Krapcho, D. Miller, A. Brest, M. Yu, J. Ruhl, Z. Tatalovich, A. Mariotto, D. Lewis *et al.*, “Seer cancer statistics review, 1975–2018, national cancer institute. Bethesda, md,” 2018.
- [2] F. A. Haggag and R. P. Boushey, “Colorectal cancer epidemiology: incidence, mortality, survival, and risk factors,” *Clinics in colon and rectal surgery*, vol. 22, no. 04, pp. 191–197, 2009.
- [3] J. G.-B. Puyal, K. K. Bhatia, P. Brandao, O. F. Ahmad, D. Toth, R. Kader, L. Lovat, P. Mountney, and D. Stoyanov, “Endoscopic polyp segmentation using a hybrid 2d/3d cnn,” in *International Conference on Medical Image Computing and Computer-Assisted Intervention*. Springer, 2020, pp. 295–305.
- [4] O. Ronneberger, P. Fischer, and T. Brox, “U-Net: convolutional networks for biomedical image segmentation,” in *Proc. of Internat. Confer. on Med. Ima. Compu. Comput.-Assis. Interven.*, 2015, pp. 234–241.
- [5] Z. Zhou, M. M. R. Siddiquee, N. Tajbakhsh, and J. Liang, “UNet++: Redesigning skip connections to exploit multiscale features in image segmentation,” *IEEE Trans. Med. Imag.*, vol. 39, no. 6, pp. 1856–1867, 2019.
- [6] D.-P. Fan *et al.*, “PraNet: parallel reverse attention network for polyp segmentation,” in *Proc. of Internat. Confer. on Med. Ima. Compu. Comput.-Assis. Interven.*, 2020, pp. 263–273.
- [7] T. Kim, H. Lee, and D. Kim, “Uacnet: Uncertainty augmented context attention for polyp semgnetation,” *arXiv preprint arXiv:2107.02368*, 2021.
- [8] A. Srivastava, D. Jha, S. Chanda, U. Pal, H. D. Johansen, D. Johansen, M. A. Riegler, S. Ali, and P. Halvorsen, “Msrf-net: A multi-scale residual fusion network for biomedical image segmentation,” *arXiv preprint arXiv:2105.07451*, 2021.
- [9] D. Jha *et al.*, “ResUNet++: An advanced architecture for medical image segmentation,” in *Proc. of Internat. Sympos. Multime.*, 2019, pp. 225–230.
- [10] Z. Zhou, M. M. R. Siddiquee, N. Tajbakhsh, and J. Liang, “UNet++: A nested U-Net architecture for medical image segmentation,” in *Deep learn. med. ima. anal. multimo. learn. clini. deci. sup.*, 2018, pp. 3–11.
- [11] D. Jha *et al.*, “Real-Time Polyp Detection, Localisation and Segmentation in Colonoscopy Using Deep Learning,” *IEEE Acc.*, 2021.
- [12] N. Ibtehaz and M. S. Rahman, “Multiresunet: Rethinking the u-net architecture for multimodal biomedical image segmentation,” *Neur. Networ.*, vol. 121, pp. 74–87, 2020.
- [13] L.-C. Chen, Y. Zhu, G. Papandreou, F. Schroff, and H. Adam, “Encoder-decoder with atrous separable convolution for semantic image segmentation,” in *Proc. of the Europ. conf. comput. vis.*, 2018, pp. 801–818.
- [14] J. Wang *et al.*, “Deep high-resolution representation learning for visual recognition,” *IEEE trans. patt. analy. mach.*, 2020.
- [15] K. Sun, M. Li, D. Liu, and J. Wang, “Igc3: Interleaved low-rank group convolutions for efficient deep neural networks,” *arXiv preprint arXiv:1806.00178*, 2018.
- [16] G. Xie, J. Wang, T. Zhang, J. Lai, R. Hong, and G.-J. Qi, “Interleaved structured sparse convolutional neural networks,” in *Proceedings of the IEEE Conference on Computer Vision and Pattern Recognition*, 2018, pp. 8847–8856.
- [17] D. Jha *et al.*, “Kvasir-SEG: A Segmented Polyp Dataset,” in *Proc. of Internat. Conf. Multimed. Model.*, 2020, pp. 451–462.
- [18] J. Bernal *et al.*, “Wm-dova maps for accurate polyp highlighting in colonoscopy: Validation vs. saliency maps from physicians,” *Computer. Medi. Imag. Graph.*, vol. 43, pp. 99–111, 2015.

- [19] K. He, X. Zhang, S. Ren, and J. Sun, "Deep residual learning for image recognition," in *Proceedings of the IEEE conference on computer vision and pattern recognition*, 2016, pp. 770–778.
- [20] S. Liu, D. Huang *et al.*, "Receptive field block net for accurate and fast object detection," in *Proceedings of the European Conference on Computer Vision (ECCV)*, 2018, pp. 385–400.
- [21] G. Huang, Z. Liu, L. Van Der Maaten, and K. Q. Weinberger, "Densely connected convolutional networks," in *Proceedings of the IEEE conference on computer vision and pattern recognition*, 2017, pp. 4700–4708.
- [22] J. Hu, L. Shen, and G. Sun, "Squeeze-and-excitation networks," in *Proc. of Comput. Vis. and Patt. Recogn.*, 2018, pp. 7132–7141.
- [23] J. Wang and other, "Deep high-resolution representation learning for visual recognition," *IEEE Trans. on Patt. Analy. Mach. Intelli.*, p. 1–1, 2020.